Inorganic Chemistry

pubs.acs.org/IC Article

Colloidal, Room-Temperature Growth of Metal Oxide Shells on InP Quantum Dots

Nayon Park, Ryan A. Beck, Kevin K. Hoang, Dylan M. Ladd, Jared E. Abramson, Ricardo A. Rivera-Maldonado, Hao A. Nguyen, Madison Monahan, Gerald T. Seidler, Michael F. Toney, Xiaosong Li, and Brandi M. Cossairt*

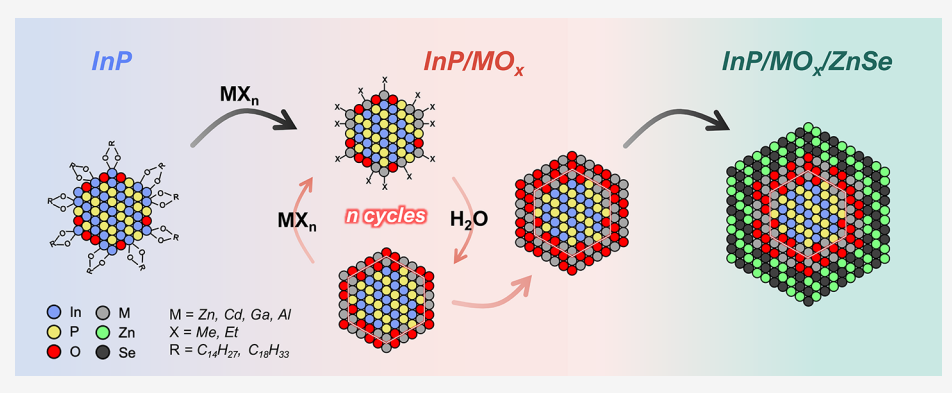


ACCESS

Metrics & More

Article Recommendations

Supporting Information



ABSTRACT: We demonstrate colloidal, layer-by-layer growth of metal oxide shells on InP quantum dots (QDs) at room temperature. We show with computational modeling that native InP QD surface oxides give rise to nonradiative pathways due to the presence of surface-localized dark states near the band edges. Replacing surface indium with zinc to form a ZnO shell results in reduced nonradiative decay and a density of states at the valence band edge that resembles defect-free, stoichiometric InP. We then developed a synthetic strategy using stoichiometric amounts of common atomic layer deposition precursors in alternating cycles to achieve layer-by-layer growth. Metal-oxide-shelled InP QDs show bulk and local structural perturbations as determined by X-ray diffraction and extended X-ray absorption fine structure spectroscopy. Upon growing ZnSe shells of varying thickness on the oxide-shelled QDs, we observe increased photoluminescence (PL) quantum yields and narrowing of the emission linewidths that we attribute to decreased ion diffusion to the shell, as supported by phosphorus X-ray emission spectroscopy. These results present a versatile strategy to control QD interfaces for novel heterostructure design by leveraging surface oxides. This work also contributes to our understanding of the connections between structural complexity and PL properties in technologically relevant colloidal optoelectronic materials.

INTRODUCTION

The utility of colloidal quantum dots (QDs), or solution-processed semiconducting nanocrystals, has expanded significantly in the past decade to lead the development of modern optoelectronics. ^{1–4} Innovations in materials synthesis, control over complex hybrid and heterostructured interfaces, and understanding the multifaceted and nuanced relationships between structure and function are at the core of this advancement. InP QDs have risen to a place of prominence and competitiveness, especially as bright and stable emitters for display and LED technologies. ^{5–7} Recent innovations in InP-based QD emitters have incorporated strategies such as surface oxide removal by HF treatment prior to shelling with a wider band gap material, ^{6,8} elimination of indium defects in the shell through extra purification steps prior to shell growth, ⁷ and careful engineering of core/shell band alignment through

tuning the core size and shell thickness^{3,5,9} or the composition of the core, the inner shell, and the outer shell layers.^{10–13}

Surface oxide defects must be considered in the design of bright and narrow InP QD emitters. Many studies have reported on both the benefits and challenges associated with oxidic species at the core/shell interface. Oxidation of InP QD surfaces is an inherent byproduct of commonly used synthetic methods. It is therefore interesting to consider how to turn this limitation into a desirable feature. In fact, it

Received: January 16, 2023 Published: April 12, 2023





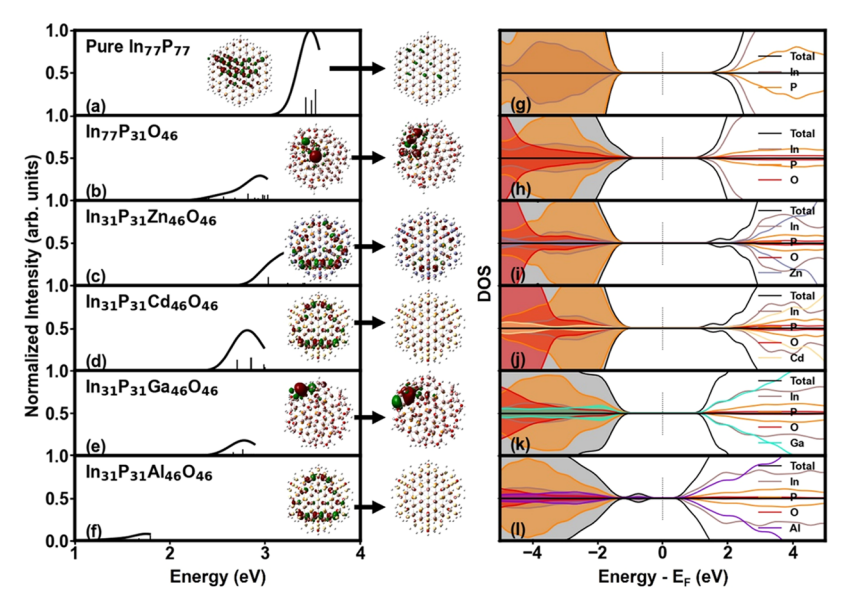


Figure 1. Linear response absorption plots for (a) pure InP and (b-f) metal-oxide-shelled InP (M = In, Zn, Cd, Ga, Al) QDs. Inset: leaving (hole, left) and arriving (electron, right) natural transition orbitals (NTOs) for the first bright (f > 0.01) excited state for each QD, shown with an isovalue of 0.02 (hole and electron delocalization indices can be found in Table S1). The projected density of states plots are shown for each system in the same order (g-l), indicating contribution from In (brown), P (orange), O (red), and total (black outline shaded in gray). Band gap reduction from pure InP and introduction of band edge states are observed with the addition of metal oxide shells. Each QD has full pseudo-hydrogen passivation to achieve an overall neutral charge.

has been demonstrated that surface oxidation can be exploited to develop some of the best-performing emitters. Some studies of interfacial surface oxides have attributed ensuing high photoluminescence quantum yield (PL QY) to reduced lattice strain and removal of interfacial defects or dangling bonds, resulting in an epitaxial core/shell interface. ^{3,14,15,19,20} In recent work reporting near-unity PL QY, water was injected with HF during synthesis, in addition to the use of highly polar, "wet" antisolvents such as ethanol and acetone during post-synthesis purification. ⁶

There is increasing consensus in the literature about the potential beneficial role of the surface phosphate layer on InP regarding its enhancement of PL QY, leading to procedures that directly introduce phosphate, water, or both, to achieve control over the core/shell interface.²¹ However, oxidic defects have simultaneously been thought to limit the PL QY in certain cases and broaden linewidths, affecting the efficiency and color purity in devices. 22,23 Single-particle spectroscopy results have demonstrated that InP linewidths are not inherently broader than CdSe, suggesting sample polydispersity needs to be controlled synthetically by not only a focus on reliable, size-controlled core growth but also uniform surface passivation and well-controlled shelling.²⁴ Computational work has also shown that exciton-phonon coupling can contribute to linewidth broadening,²⁵ and this effect is exacerbated by incomplete surface passivation and structural disorder caused by defects.²² Therefore, understanding how to precisely control and improve the InP QD surface and interfacial structure, together with the optical properties, will be facilitated by the development of a new synthetic approach that is attuned to the atomic level detail at the QD surface.

In light of the need for atomically precise control over surface structure and stoichiometry, there has been growing interest in the field to explore layer-by-layer growth of heterostructures. ^{5,26–29} Talapin et al. have demonstrated the synthesis of "digital" nano-heterostructures through colloidal

atomic layer deposition (c-ALD), inspired by the conventional method of solid film deposition. ^{26,27} While conventional ALD leverages repeated cycles of alternating self-limiting reactions in the vapor phase, c-ALD relies on the phase change of nanomaterials in liquids and requires preservation of colloidal stability between transfer steps. ²⁷ In ALD, purge steps in between precursor additions are important for ensuring excess reagents are removed and layer-by-layer growth is conformal and uniform on a substrate. Using similar motifs, Klimov et al. have demonstrated the formulation of interlayers between core/shells to achieve monolayer deposition control. ³⁰ Like ALD, they used evacuation steps between each addition to remove the excess precursors.

Here, we demonstrate a facile, room-temperature procedure for colloidal metal oxide shelling of InP QDs. First, we show using theoretical modeling that surface oxides on InP QDs are detrimental to bright and narrow linewidth PL as they introduce nonradiative recombination pathways. We then compare these structures with other monolayer metal oxide shells on InP QDs (M = Zn, Cd, Ga, Al) and find that ZnO and CdO shells, unlike GaO and AlO shells, reduce the nonradiative rate and result in a density of states near the valence band maximum (VBM) that looks similar to that of defect-free, stoichiometric InP QDs. The choice of these metals was guided by their common use in InP QD alloys and in the passivating shells of III-V heterostructures. Inspired by these results, we employed reagents commonly used for ALD to systematically grow metal oxide shells on InP QDs. This new method introduces a colloidal, layer-by-layer shelling approach using surface-limited reactions by combining elements of both ALD and successive ionic layer adsorption and reaction (SILAR) and is generalizable to many metal oxides. The presence of a thin metal oxide shell is evident from the first precursor addition step by powder X-ray diffraction (pXRD) and extended X-ray absorption fine structure spectroscopy (EXAFS). Repeated cycles of precursor addition

promote continued growth without changing the InP core stoichiometry. To investigate the impact of the metal oxide interfaces on PL properties, we have synthesized and compared the resultant PL of InP/ZnSe core/shell QDs with those that have metal oxide interfaces, where consistent enhancement in the PL QY was observed. Furthermore, a narrowing of the PL linewidth was attributed to the larger kinetic barrier for ions to diffuse across the oxide shell layer, resulting in a reduction of oxidized P as determined by X-ray emission spectroscopy (XES). These results suggest the oxophilicity of interfacial atoms as an important factor to consider in controlling optoelectronic properties. These results also present a facile and versatile strategy to finely tune and leverage oxidic defects at the core/shell interface as we gain a deeper understanding of the design principles for improved emission properties of QD materials.

RESULTS AND DISCUSSION

Investigation of the Effects of Surface Oxide through Computational Modeling. The prevalence of oxidic surface species in InP QDs and their impact on optoelectronic properties have generated many empirical studies probing and controlling the average extent of P oxidation, typically measured by solid-state ³¹P NMR spectroscopy, ^{16,17} with the goal of improving optical properties. While a mixture of oxidic species such as phosphate, polyphosphate, metal hydroxide, and metal oxide may be present at the InP QD surface, it is not clear that they are all detrimental to PL QY when present at the core/shell interface. An attempt at modeling this system would mean making some critical assumptions, such as randomly distributing the oxides both spatially and in terms of their speciation at the InP QD surface. Computational studies have thus far focused on InP cores and epitaxial core/ shells assessing the effects of stoichiometry or incorporation of GaP interlayers, 31-33 besides one study that reported on the use of a slab geometry with stoichiometry In₈P₈O₄ to show reduced lattice constant and a smaller band gap as a result of InP QD surface oxidation.³⁴

We constructed an In₃₁P₃₁/In₄₆O₄₆ cluster model, wherein an InP core is fully passivated by a monolayer indium oxide shell, to compare with pure In₇₇P₇₇. Images of the optimized models can be found in Figure S1 and the xyz files are provided as Supporting Information. All clusters are terminated by pseudo-hydrogen atoms to give In₇₇P₇₇H₁₀₈ or In₃₁P₃₁M₄₆O₄₆H₁₀₈ compositions to reduce exaggerated surface effects associated with small cluster models. The corresponding linear response absorption spectra are presented in Figure 1a,b. In the oxidized InP core (InP/InO), surface P atoms of the In₇₇P₇₇ parent cluster were replaced with O atoms. Realistically, oxide coverage in as-synthesized InP QDs is far less than a complete shell (12% phosphate species measured by Chaudret et al. 16 using solid-state NMR), and for our samples synthesized from InP magic-sized clusters (MSC), we measured 16% oxidized phosphorus after synthesis by phosphorus X-ray emission spectroscopy (XES, Figure 3b), indicating the presence of phosphate that is not explicitly accounted for in this model.

Compared to the stoichiometric, defect-free $In_{77}P_{77}$ core, which shows an abrupt band gap and strong absorbance at 3.4 eV (Figure 1a,g), $In_{31}P_{31}/In_{46}O_{46}$ exhibits a reduced band gap and emergence of dark states near the band edges (Figure 1b,h). Based on the natural transition orbitals (NTOs), the monolayer indium oxide shell localizes charge density at the

InP/InO interface (Figure 1b, inset). The projected density of states plot for the InP/InO system shows the contribution of P and O to the valence band, which indicates that at the band edge, the phosphorus component dominates while the oxygen component appears more prominently deeper into the valence band, which is consistent with oxygen being more electronegative (Figure 1h). There is some contribution near the VBM from indium, which is attributed to the covalent mixing of In and O, giving rise to dark absorption states (f < 0.001). Dark states near the band edges have been associated with unfavorable phenomena such as PL blinking and linewidth broadening. ^{22,35-37} In order to quantify the impact of the dark states on the optical properties of the modeled systems, the ratio of the magnitude of the first-order nonadiabatic coupling between the ground and first excited states, |d|, was examined for each of the clusters (Figure S2). The rate of nonradiative relaxation is proportional to $|d|^2$, $^{38-40}$ and thus in the case of InP/InO, it can be determined that the rate of nonradiative decay is larger than that of the pure InP core. Therefore, an InP core with a natively oxidized surface is expected to be a poor starting material for fabricating bright and narrow emitters and motivates us to eliminate these defects or otherwise leverage them to form a more favorable interface.

Additional metal-oxide-shelled structures were constructed by replacing the surface In with a divalent or trivalent metal (M = Zn, Cd, Ga, Al) and the surface phosphorus with oxygen (Figure S1). These metals were chosen for their relevance as alloy and shelling materials for InP. 9,41-43 The resulting models have a general formula of In₃₁P₃₁/M₄₆O₄₆. Regardless of the bulk stoichiometry of the metal oxides, the metal-tooxygen ratio is 1:1. Pseudo-hydrogens were used to charge balance at the surface in order to achieve neutrally charged models, as detailed in the Supporting Information (Text S1). The divalent metal oxide shells on the InP core (i.e., ZnO and CdO) exhibit a reduced band gap, and thus a red-shifted absorption (3.0 and 2.7 eV, respectively) (Figure 1c,d,i,j) compared to the pure InP core of the same size (3.4 eV). Unlike InP/InO, both ZnO and CdO shells give rise to a high density of states near the VBM with strong P contribution much like those of pure InP. This effect is accompanied by a reduction of the nonradiative rate compared to both InP/InO and pure InP (Figure S2). In both the InP/ZnO and InP/CdO structures, new states can be seen to emerge near the edge of the conduction band (Figure 1i,j). The states arising from the CdO shell extend further into the band gap than in the case of a ZnO shell, which can be explained by the contribution of the Cd 4d states that lie lower in energy than the Zn 3d orbitals. Based on these results, ZnO and CdO shells on InP are promising candidates to replace indium oxide surfaces for improving the optical properties of bright InP-based core/shell QDs. Interestingly, these findings may be related to the PL enhancement of InP QDs upon surface treatment using Zn or Cd carboxylate. 44,45 In a recent study using dynamic nuclear polarization surface-enhanced nuclear magnetic resonance spectroscopy (DNP SENS NMR), InP QDs exhibiting high quantum yield (30-60%) as a result of Cd carboxylate surface treatment were found to have a mixture of phosphate species and Cd alloying at the surface. 45 The surface environment of Zn or Cd carboxylate-capped InP QDs is expected to be analogous to that of the corresponding monolayer metal oxides in the first coordination shell.

For the InP core shelled with either gallium or aluminum oxide, the change in the density of states from the

stoichiometric, defect-free In₇₇P₇₇ core is seen more prominently at the VBM (Figure 1k,l). This was also the case for In₃₁P₃₁/In₄₆O₄₆ as previously discussed. The GaO- and AlOshelled structures show surface-localized states near the VBM that have reduced contribution from P at the band edge and a relative increase in the contribution from the added metal and oxygen. Both InP/GaO and InP/AlO are expected to exhibit faster nonradiative decay (Figure S2), given the presence of the band edge defect states caused by the oxide layer. The first bright states in these systems are calculated to be at 2.6 eV for GaO and 1.1 eV for AlO (Figure 1e,f). The NTOs for the transitions for all systems are shown in Figure 1a-f insets. The InP/InO, InP/GaO, and InP/AlO systems have localized defect-like states near their surface compared to the pure InP, InP/CdO, and InP/ZnO systems. The localized defect-like surface states result in a much higher ratio of the nonradiative rates and are not expected to yield high-performing emitters. Another factor to consider regarding surface defects is that the local electron count at the interface is more significantly disrupted due to the off-stoichiometric composition of group III oxides in our models, even though charge compensation is achieved at the surface by the pseudo-hydrogens.

Additionally, we have explored $In_{31}P_{77}M_{46}$ (M = Zn, Cd, Ga, Al) structures, where only the surface In atoms are replaced by other metals without the oxides. Examining the electronic structure of these systems reveals that the impact on the absorption features and nonadiabatic coupling is stronger when there is an oxide layer present than with any of the metals by themselves (Figure S3). We observed clean band gaps for all structures with an increased band gap for In₃₁P₇₇Ga₄₆ and $In_{31}P_{77}Al_{46}$ and a reduced band gap for $In_{31}P_{77}Zn_{46}$ and In₃₁P₇₇Cd₄₆. These results highlight that the surface oxides play an influential role in the electronic structure and the resultant optical properties and should be considered together with the identity of the metal on the surface of the core QDs. Furthermore, while the computational results do not suggest that any metal oxide shell would be an improvement over pure, defect-free InP, they do suggest that the divalent metal oxides may result in improved optoelectronic properties compared to trivalent metal oxides. Instead of eliminating the oxides entirely, which is challenging and may be impossible under certain conditions, we pursued development of a generalizable synthesis of metal oxide interfaces and compared their resultant optical properties.

Growth of Metal Oxide Shells on InP QDs. Synthesis and Surface Chemistry. The colloidal growth of metal oxide shells on InP QDs starts with the addition of alkyl metal to the QD solution and continues through alternating additions of alkyl metal and water with vacuum purge and redissolution steps in between (Figure 2). InP QDs were prepared from carboxylate-capped InP magic-sized clusters used as a single-source precursor. 46,47 The resulting InP QDs were purified by multiple precipitation—centrifugation—redissolution cycles fol-

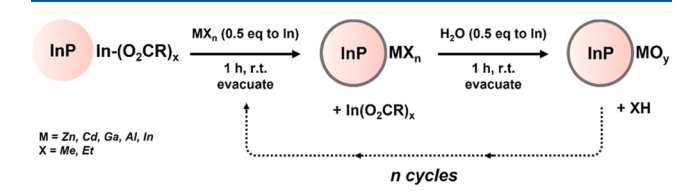


Figure 2. Colloidal growth of metal oxide shells on carboxylate-capped InP QDs ($R = C_{13}H_{27}, C_{17}H_{33}$).

lowed by size-selective gel permeation chromatography. An InP QD stock solution was then prepared in toluene with a known In concentration, where the optical density is 0.197 for a 10 mL stock solution containing 0.057 mmol of In.

To a solution of InP QDs, alkyl metal (M = Zn, Cd, Ga, Al, In) was added at 0.5 equiv relative to the total mmol of In. With the estimate that approximately 50% of In atoms are on the surface for 3 nm diameter InP QDs, 0.5 equiv of alkyl metal approximately corresponds to 1:1 surface In to M. A typical scale of reaction used 0.04 mmol of In in the InP QD stock solution. While striving toward full characterization of all resultant metal-oxide-shelled QDs, we chose to follow the growth of the ZnO-shelled structure more closely as a representative system for a more detailed understanding of the surface chemistry. At room temperature, diethyl zinc reacts with the InP QD surface by exchanging with surface indium carboxylate or adsorbing onto surface oxide or phosphate species to form metastable surface metal-alkyl bonds (broad resonance from ethyl group centered around δ = 0.2 ppm, Figure 3a,e). Diethyl zinc also reacts with carboxylic acid adsorbed to the InP surface to produce ethane ($\delta = 0.8$ ppm) and desorbed metal carboxylate (sharp oleate resonance $\delta \sim$ 5.6 ppm) (Figure 3a,e). Previous studies with CdSe QDs used CdMe₂ and ZnEt₂ to remove excess carboxylic acid and other acidic impurities and reported on surface-bound methyl groups along with free metal carboxylates and methane or ethane.⁵⁰ There is no change in the ¹H NMR spectra after the first spectrum is taken at 10 min, indicating the reaction has gone to completion by that time. Addition of ZnEt₂ up to 2 equiv relative to total In (i.e., in excess of available surface sites) shows a combination of free ZnEt2 and bound alkyl features around 0.2 ppm (Figure S4). This indicates that the reaction is self-limiting, a characteristic feature of half-reactions in ALD. After all of the surface sites are consumed in the reaction with alkyl metal, the reaction no longer proceeds. At this point, InP QDs remain colloidally stable in toluene and can be redissolved in other nonpolar solvents such as 1-octadecene (ODE). To remove any excess alkyl metal, the system was evacuated to complete dryness. At this step, it is important to note for safety that the cold traps should be removed with care and the pyrophoric alkyl metal reagents be quenched appropriately with a bleach solution. Creating a separate hazardous waste stream distinct from routine waste should be considered for proper disposal.

Upon redissolution of the alkyl metal treated QDs in toluene, water was injected in the same molar equivalent as the alkyl metal and stirred at room temperature. At this step, we no longer observed features associated with ZnEt₂ or the surfacebound ethyl groups by ¹H NMR spectroscopy. Instead, the alkene region showed the presence of both bound oleate and unbound In or Zn carboxylate (bimodal peak between 5.4 and 5.7 ppm, Figure 3a). This was consistently observed throughout two cycles, where upon ZnEt2 addition, metal oleates dissociate from the QD surface and become "free", while the addition of water partially re-coordinates the oleates back to the QD surface (Figure 3a,e). We hypothesize that the re-coordination of oleate is due to the dynamic exchange with surface hydroxide which forms upon the reaction of surface alkyl and water. Upon completion of the reaction, evacuation and redissolution steps can be repeated to restart and continue the metal oxide shell growth cycles or the reaction can be halted at one cycle.

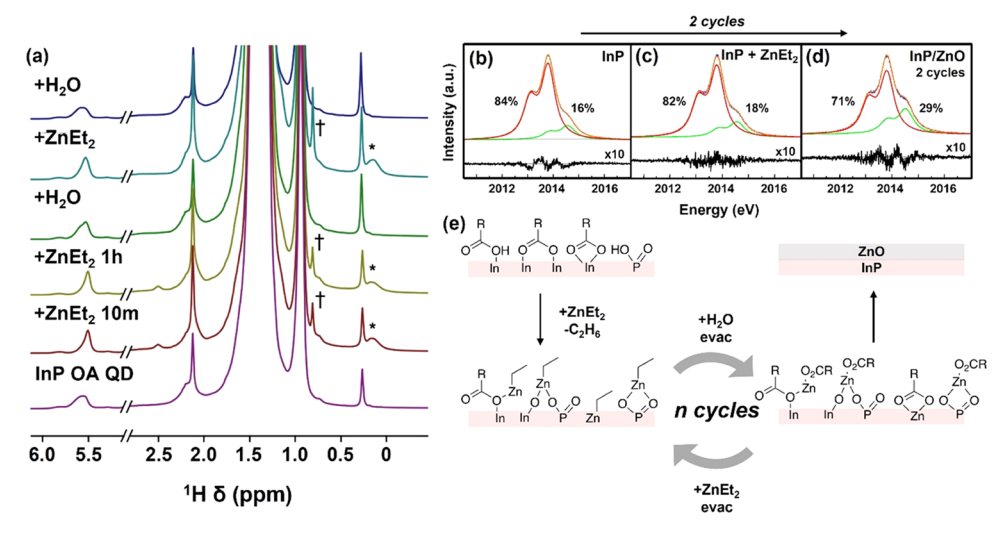


Figure 3. (a) 1H NMR spectrum showing the broad resonance of metastable surface-bound ethyl groups (*) and the evolution of ethane (†) upon the self-limited reaction of ZnEt₂ with the InP QD surface. The sharpening of the oleate alkene peak ($\delta \sim 5.6$ ppm) indicates desorption of oleate, which is then observed to re-coordinate upon the addition of H₂O. (b–d) Phosphorus XES spectra of InP QDs (b) as-synthesized, (c) after ZnEt₂ addition, and (d) after two cycles of ZnEt₂ and H₂O addition, fit with a linear combination (orange) of phosphide (red) and phosphate (green) components with the percentage for each P oxidation state noted. The residual signal after fitting (10×) is shown in black. (e) Proposed reaction scheme for the reaction of ZnEt₂ and H₂O at the InP QD surface leading to ZnO shell growth.

We probed the local environment of phosphorus in the metal-oxide-shelled InP QDs using P K α and K β X-ray emission spectroscopy (XES). P XES is an especially useful tool for observing and quantifying P speciation and has been used previously for the characterization of InP-based QD systems. 18 P K α XES shows that the addition of ZnEt₂ results in no change in P oxidation (Figure 3b,c). After two cycles, the bulk fraction of oxidized P increased by 13% for ZnO (Figure 3d). Similar results were observed for CdO and GaO, shells, where the addition of alkyl metal had a negligible change on the P oxidation level, and the addition of water to complete the cycle led to an increase in P oxidation (Figure S5a-d). The phosphate fingerprint in the K β spectrum at 2124 eV was consistently observed for all samples in agreement with the K α data (Figure S5e). There is no oxidant present for P upon the addition of alkyl metal, resulting in no increase in the phosphate fraction. However, with the induction of shell growth following the addition of water, we start to observe an increase in P oxidation. Photooxidation by water on InP QD surfaces was previously reported to originate from O²⁻ forming interstitial defects in the lattice.²²

Figure 3e illustrates the representative scheme of the surface chemistry throughout the ALD-like reaction cycles for layerby-layer growth of ZnO on the colloidal InP QD surface. The native surface of InP QDs is composed of In carboxylate ligands coordinated in a mixture of bridging, bidentate, and monodentate binding modes. 51,52 Some phosphate species are also expected to be present at the surface. The addition of ZnEt2 strips off some of the bound oleate species from the surface concomitant with the formation of surface-bound ethyl groups as shown by the ¹H NMR spectrum (Figure 3a). Zn ethyl species are proposed to coordinate surface P following displacement of In carboxylate. Additionally, Zn ethyl species may coordinate to the surface phosphate, oxides, or carboxylates coordinated to In. The proposed surface coordination environment is consistent with that previously elucidated for InP treated with divalent cations like Cd using solid-state dynamic nuclear polarization NMR spectroscopy.

Free carboxylic acids that are not removed by purification and are in dynamic exchange with the surface-bound carboxylates will also react with ZnEt₂ to evolve ethane and produce Zn ethyl carboxylate species that can coordinate to the InP QD surface. The addition of water shows evidence for recoordination of oleate ligands and the desorption of the surface-bound ethyl groups. This indicates that the oleates are now re-bound to the surface In or Zn by replacing the ethyl group and evolving ethane. We propose that repeating these cycles leads to colloidal layer-by-layer growth of metal oxide using the InP QD surface as the substrate.

The evacuation step between reagent additions is crucial for preventing independent nucleation of metal oxide and ensuring that the reaction is limited to the surface of the InP QDs. A significant excess of either reagent involved in the metal oxide growth can also result in the loss of colloidal stability and degradation of the QDs. Furthermore, at an elevated temperature (200 °C), gray precipitates formed which were confirmed to be Zn⁰ particles by XRD (Figure S6). Therefore, rather than using precursors in excess and relying on the purging steps for their removal between cycles, judicious amounts are employed at each addition as in SILAR shell growth. Furthermore, an attempt to grow thicker ZnO shells eventually crashed out the QDs after the addition of 6.2 equiv ZnO (equivalent to ~1 unit cell monolayer of ZnO on 3 nm diameter InP QD, see Text S2 for details). The aggregates exhibited wurtzite phase ZnO with 6.4 nm diameter by Scherrer analysis and 4.3 nm by transmission electron microscopy (TEM) (Figure S7). The loss of the zinc blende InP pattern suggests that a thicker ZnO shell has grown on the InP QDs, but these data do not explicitly rule out independent nucleation of wurtzite ZnO nanoparticles. This growth procedure for a thicker shell could be further optimized by adding extra ligands as previously demonstrated with AlMe₃ on a wide range of NC systems.^{28,2}

Bulk Structural and Optical Characterization. Growth of metal oxide shells is indicated by transmission electron microscopy (TEM). While the size of InP QDs remains at

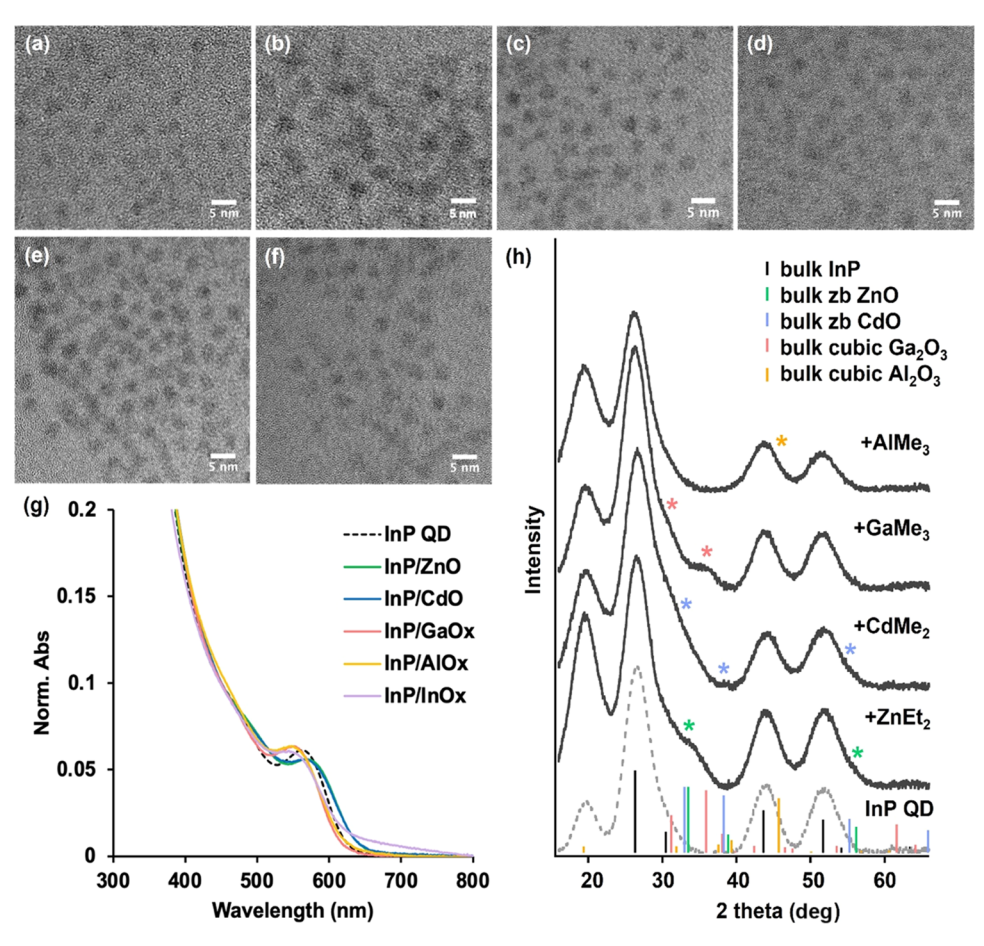


Figure 4. (a) TEM images of (a) InP + ZnEt₂ (3.0 ± 0.4 nm), (b) InP/ZnO two cycles (3.7 ± 0.5 nm), (c) InP + CdMe₂ (3.0 ± 0.4 nm), (d) InP/CdO two cycles (3.4 ± 0.4 nm), (e) InP + GaMe₃ (3.0 ± 0.3 nm), (f) InP/GaO_x two cycles (3.6 ± 0.5 nm), (g) overlay of absorbance spectra of InP/MO_x upon two cycles of metal oxide shelling, and (h) XRD pattern of InP QDs treated with alkyl metal. The simulated patterns show the appearance of new broad features that are consistent with the zinc blende or cubic lattice patterns of the metal oxide and with the experimental data (notable, corresponding features are shown with an asterisk (*) of the same color as bulk pattern). InP (PDF #00-032-0452), ZnO (PDF #03-065-2880), CdO (PDF #00-005-0640), Ga₂O₃ (PDF #00-006-0529), Al₂O₃ (PDF #00-050-0741).

the starting 3 nm diameter after the first alkyl metal addition, after two cycles of alkyl metal and water additions, an increase in the QD size was observed (Figure 4a-f). We measured a 0.7 nm increase after two cycles for ZnO, 0.4 nm for CdO, and 0.6 nm for GaO_x accounting for approximately 0.5 unit-cell-thick layers. The increase in size was observed without a change in the QD morphology or core stoichiometry as determined by elemental analysis (Table 1). As expected, the ratio of metal introduced by alkyl metal relative to In increases between the first and the second cycle. The ratio of P relative to In remains mostly constant or showed a small decrease, supporting that the InP core is intact throughout shelling and that a diverse set of surface reactions resulting in alkyl coordination at the surface occurs (as discussed above and depicted in Figure 3e) besides In carboxylate to alkyl metal exchange, which would result in a higher P ratio. Across all of the samples, the cation (In, M) to anion (P) ratio is between 2.4 and 5.3, consistent with the presence of the expected oxides as required by charge balance.

At each step of layer-by-layer shelling of metal oxide on InP QDs, changes in the optical absorption and photoluminescence were also observed (Figure S8a-e). Notably, a redshift in the absorption spectra was observed for the divalent metal oxides ZnO and CdO, while a blueshift was observed for the trivalent metal oxides GaO_w AlO_w and InO_x (Figure 4g). The

Table 1. Elemental Compositions of InP and InP/MO_x QDs Obtained from Inductively Coupled Plasma-Optical Emission Spectrometry (ICP-OES)^a

	In	P	Zn	Cd	Ga	Al	M/P
InP QD	1.5	1					
$+ZnEt_2$	1.6	1	1.1				2.7
$ZnO \times 2$	1.6	1	3.5				5.1
+CdMe ₂	1.7	1		0.7			2.4
$CdO \times 2$	1.7	1		1.6			3.3
+GaMe ₃	1.6	1			1.2		2.8
$GaO_x \times 2$	1.7	1			2.5		4.2
+AlMe ₃	1.3	1				1.9	3.2
$AlO_x \times 2$	1.5	1				3.8	5.3
+InMe ₃	3.2	1					3.2
$InO_x \times 2$	5.1	1					5.1

^aThe molar ratios are normalized to moles of P. The ratio of total metal atoms to P is noted.

redshifts for ZnO and CdO are consistent with our theoretical predictions, wherein dark states appear near the band edges. Further, this redshift may be a sign of softening of the electronic confinement. In the case of the blueshift observed with AlO_x, GaO_x, and InO_x, our density functional theory (DFT) calculations showed the emergence of localized surface

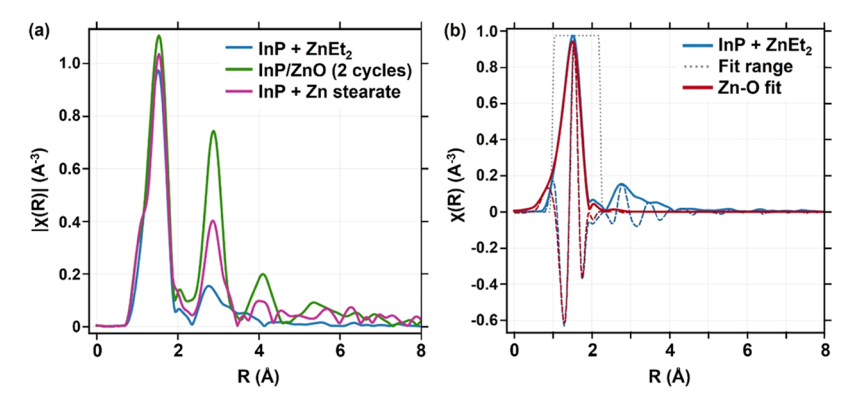


Figure 5. Zn K-edge EXAFS of ZnO-shelled InP QDs. (a) InP + ZnEt₂ (blue), InP/ZnO after two cycles (green), and InP + Zn stearate (magenta). All samples show a characteristic Zn-O bonding environment in the first coordination shell characterized by a peak near R = 1.5 Å. (b) First coordination shell of InP + ZnEt₂ (blue) fit in real space by a single degenerate Zn-O scattering path model (red), showing both the real component (dashed lines) and magnitude (solid lines) of the Fourier transform. Fit parameters are listed in Table S2.

states at the band edges, which may manifest as stronger confinement. The DFT calculations also indicated that the addition of Al, Ga, and In resulted in an overall increase in band gap, so the observed blueshift in the experiment may be reflective of incomplete oxidation of the outer trivalent metal layer and/or alloying at the InP/MO_x interface.

Increases in PL or PL quenching (from ~1% PL QY of the starting InP QD cores) were observed with the first alkyl metal addition step (Figure S9). Following the PL intensity throughout two addition cycles of ZnO, we correlated quenching of PL with the carboxylate being stripped from the InP QD surface and recovery of PL with the recoordination of the carboxylate in tandem with the ¹H NMR results discussed earlier (Figure 3a). The literature precedent for conventional ALD on InP QD films reported quenching of PL with alkyl metal and then recovery of PL upon addition of water.⁵³ At the completion of the second cycle, significant quenching was observed for both ZnO- and CdO-shelled InP QDs, while the sample treated with GaMe3 and water maintained higher PL intensity than the original InP QD sample. Besides the prevalence of surface-localized dark states due to metal oxide shell predicted by theory, the lattice mismatch between the metal oxide shell and InP core may be an important factor to consider, even though these shells are very thin to fully take into account the effects of strain and lattice mismatch (a = 0.463 nm for zinc blende ZnO, 0.470 nm for zinc blende CdO, and 0.587 nm for zinc blende InP). Previous studies examining the reaction of alkyl metal reagents with CdSe QDs have reported on a photoinduced absorption bleach as a signature for n-doping by alkyl radicals. 50,54 In our case, we did not observe photoinduced doping, but instead under ambient light, the surface alkyl groups were intact and likely in dynamic exchange with the free carboxylates.

The powder XRD patterns of metal-oxide-shelled InP QDs showed the broad, characteristic (111), (220), and (311) peaks of bulk zinc blende InP (Figure 4h). Additionally, new broad diffraction peaks corresponding to zinc blende or cubic phase metal oxide emerged as early as the first addition of alkyl metal. Typically for core/shell nanocrystals, the growth of the shell can be evidenced in powder XRD by changes in the peak linewidth and shifts based on the weighted contribution of the core and shell lattice structures, taking into account scattering factors, where materials with a smaller scattering factor contribute more weakly. With a thin, one or sub-monolayer shell, peak broadening and minimal shifting toward the bulk

pattern of the shell structure are expected. In the InP/MO_x QDs, the metal oxide features can be seen near 34° for ZnEt₂ treatment, 33° for CdMe2, and 31 and 36° for GaMe3. In addition to the new peaks, peak broadening and increased intensity for zinc blende InP(220) and (311) peaks at 44 and 52° were also observed. Comparing the XRD patterns after first alkyl metal addition and after two cycles for CdO- and GaO_x-shelled InP QDs indicates growth in the average crystalline domain size (Figure S10), consistent with the increased particle size. It is also notable that additional shoulders and peaks observed for other thin shells of metal oxides are not present for the AlO, shell where no features other than the increased intensity of the peak at 46° are observed. The broad peak around 20° that appears for all samples is indicative of the surface organic ligands, with density, ordering, and ligand length contributing to the peak intensity and the linewidth. 50

The powder XRD patterns were simulated using the DebyeByPy simulation package developed by Trigg⁵⁷ and show good agreement with the experimental data (Figure S11a). The simulated patterns for metal-oxide-shelled InP QDs show distinct patterns, and the new features and peak broadening are suggestive of zinc blende or cubic patterns of the respective metal oxide. Notably, these observations from $In_{31}P_{31}/M_{46}O_{46}$ structures are different from those shown by the $In_{31}M_{46}P_{77}$ structures, where only shifts in the peaks were observed toward higher angles as expected based on the smaller size of the metal cations, which result in lattice contraction (Figure S11b).

We note that the cubic phase of gallium oxide seems to give the best qualitative match with our experimental and simulated patterns (Figures 4h and S10a). While various polymorphs of gallium oxide are known, growth of cubic (δ) phase Ga₂O₃ thin film has yet to be reported.⁵⁸ Given that substrate lattice and growth temperature are the most important factors in determining the formation of a particular gallium oxide polymorph, 58 we hypothesize that the zinc blende InP core with spherical curvature serves as a unique template for metal oxide growth at monolayer to sub-monolayer shell thickness, instigating metal oxide deposition reminiscent of zinc blende or cubic phase even when it is not the thermodynamically favored phase. Similar phenomena have been previously reported in QD systems where the crystal structure of a HgS interlayer and an outer CdS shell was dictated by the wurtzite CdSe core in layer-by-layer shell growth.³⁰ Additionally, sub-

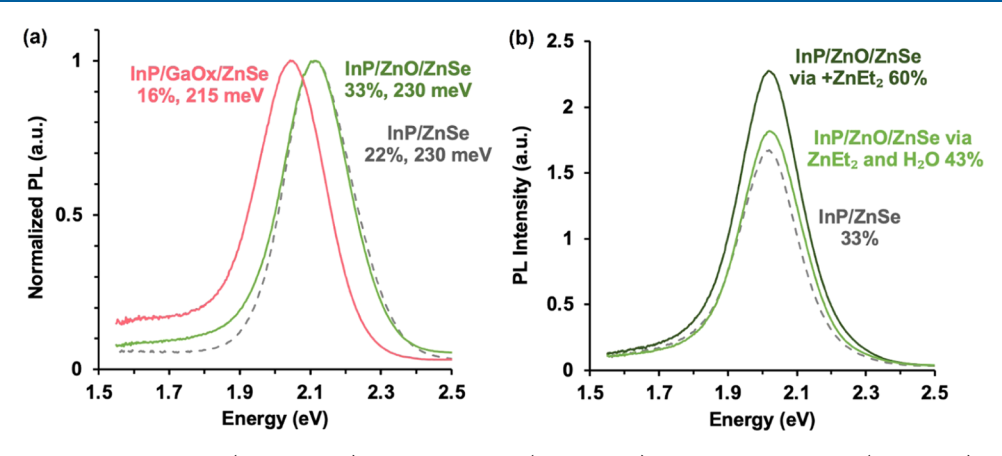


Figure 6. (a) Normalized PL of InP/ZnSe (gray, dashed), InP/ZnO/ZnSe (green, solid), and InP/GaO_x/ZnSe (pink, solid) with thin ZnSe shells to compare their emission linewidths (noted in meV along with quantum yield in %) and (b) relative PL and PL QY (%) of InP/ZnSe (gray, dashed), InP/ZnO/ZnSe treated with only ZnEt₂ (dark green, solid) and ZnEt₂ and water (green, solid) prior to shelling with thicker ZnSe shells. The shell grown here used 5 equiv ZnSe to mmol In and is expected to have a \sim 2 unit cell monolayer thickness.

monolayer thicknesses of metal oxide shells can be expected to result in preferred growth in some facets over the others, which would explain why not all peaks of metal oxides are represented in the XRD of the thin metal-oxide-shelled InP QDs.

In the case of the ZnO shell on InP QDs, the growth of zinc blende ZnO peaks is suggested by XRD upon first addition of diethyl zinc. After two cycles of ZnO deposition, the wurtzite phase ZnO pattern appears, which is the thermodynamically favored phase of ZnO (Figure S7a). Similar to cubic phase Ga_2O_3 , the growth of zinc blende ZnO may be instigated using the zinc blende InP core as a template for growth, after which the wurtzite lattice prevails. Unlike the CdO and GaO_x shells where a more gradual increase in peak intensity and broadening are observed, the appearance of more distinct and sharper peaks of wurtzite phase ZnO may suggest independent nucleation of ZnO nanoparticles in addition to ZnO shell growth on InP QDs.

We further probed local Zn bonding environments using extended X-ray absorption fine structure spectroscopy (EXAFS) at the Zn K-edge. Transmission data processing, transformation, and fitting with FEFF8 were completed using XAS Viewer within the Larch data analysis package. 59 We compared three InP QD samples each treated with ZnEt2, two cycles of ZnEt2 and water, and Zn stearate. InP QDs treated with Zn carboxylate have been extensively studied for their high QY, 44,60 and the Zn carboxylate ligand shell was of interest as it emulates the first coordination sphere environment of a metal oxide shell. From the first addition step of diethyl zinc, the presence of predominantly Zn-O bonding is indicated by the primary coordination shell peak near R = 1.5Å (Figure 5a). This is supported by real-space fitting results when modeled by a single Zn-O scattering path from bulk wurtzite ZnO with a Zn-O coordination number of about 3 and a Zn-O bond length of about 2.0 Å (Figure 5b and Table S2). This is consistent with our observation that the alkyl metal treatment alone instigates the deposition of a thin metal oxide shell on InP QDs. Fitting a two-path model of Zn-O (bond length of 2.0 Å) and Zn-P (bond length of 2.4 Å)⁶¹ and allowing both coordination numbers to vary result in a Zn-P coordination of effectively zero. This suggests Zn-P bonds represent less than 10% (approximate detection limit for this measurement) in the Zn first coordination sphere constituents (Figure S12a,b). The peak at R = 1.5 Å is consistent across the

three InP QD samples, suggesting a similar prevalence of Zn–O bonding (Figure 5a). Indeed, modeling the InP/ZnO (two cycles) sample by the same single Zn–O path results in a statistically improved fit compared to InP + ZnEt₂ (Table S2).

Accurately modeling the secondary shell coordination sphere ($R \approx 2.8 \text{ Å}$) of Zn is impeded by the uncertain structure of the core/shell interface and high surface-to-volume ratio of the nanoparticles. The comparatively low-amplitude peak in InP + ZnEt2 is likely a result of a wider distribution of bond lengths and varied secondary coordination sphere constituents that destructively interfere when represented in $|\chi(R)|$. A qualitative model demonstrating this is offered in Figure S12c. The secondary sphere peak in InP + Zn stearate and InP/ZnO samples (Figure 5a) is well described by the Zn-Zn scattering path in bulk ZnO (Figure S12d). Thus, EXAFS results are consistent with the proposed surface chemistry and shell growth (Figure 3e). However, caution is taken in the interpretation of these Zn K-edge EXAFS results as the growth of a ZnO shell is not particularly discernible from the possible independent nucleation of ZnO particles.

Upon comparing these structures with Zn-carboxylatecapped InP QDs, we found that the coordination shells of Zn-carboxylate-capped InP QDs display Zn coordination environments somewhere in between the other two samples. If the surface environment and passivation provided by Zn carboxylate are effective at PL increase but easily removed by further surface manipulations, our approach of layer-by-layer deposition of metal oxide may provide a solution for epitaxial growth and careful control of the surface and electronic structure. The composition of these QDs was further investigated by energy dispersive X-ray (EDX) spectroscopy, where co-localization of In and Zn was observed. For this, it was important due to the instability of the nanoparticles under the intense electron beam that the nanoparticles were shelled with silica to achieve stable imaging (Figure S13). Whether wurtzite ZnO nanoparticles were independently nucleated or deposited on InP QDs as a highly crystalline shell remains inconclusive, and this data may suggest both processes are occurring simultaneously.

Additionally, after two cycles, AlO_x-shelled QDs were quick to lose colloidal stability, precluding more insight from the acquired patterns or continued shelling. Unlike other alkyl metals, the addition of InMe₃ resulted in the appearance of sharp and distinct peaks in the XRD pattern that conceivably

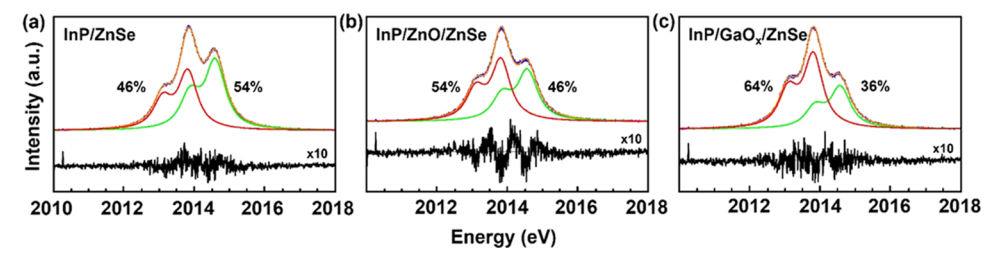


Figure 7. Phosphorus XES of (a) InP/ZnSe, (b) InP/ZnO/ZnSe, and (c) $InP/GaO_x/ZnSe$ showing the phosphide (red) and phosphate (green) components that make up the linear combination of the data and fit. ODE-Se was used as the Se precursor in the synthesis to avoid convolution from additional P oxidation from TOP-Se. The spectra were fit with a linear combination (orange) of phosphide and phosphate components with the percentage for each P oxidation state noted. The residual signal $10\times$ trace after fitting is shown in black.

correspond to $\rm In_3(PO_4)_2$, suggesting a surface that can be described as oxyphosphate or polyphosphate (TEM and XRD for Al and In can be found in Figure S14). Other reagents should be explored for layer-by-layer shelling with $\rm In_2O_3$. Furthermore, sharp peaks from the crystal pattern of long-chain hydrocarbon (paraffin) were evident in samples that were not purified by gel permeation chromatography (Figure S15). This could simply be avoided by purification via gel permeation chromatography for the removal of ODE and other impurities. Adventitious crystallization of long-chain carboxylates is likely affecting the surface chemistry and embedding in the ligand shell.

Effect of MO_x Interface in InP/ZnSe Core/Shells. Next, we explored the impact of these controlled metal oxide interfaces on the optoelectronic properties of InP/ZnSe core/ shell QDs. We were interested in the ZnO and GaO_x shells in particular for their PL properties after treatment with alkyl metal and previous studies on various Zn- and Ga-based interlayers in InP/Zn(S,Se) core/shell systems. 10,62,63 A thin shell of ZnSe was applied at 1.5 equiv Zn and 0.8 equiv Se relative to mmol In in the InP QD core (calculated from a stock solution) that was treated with diethyl zinc or trimethyl gallium. Previously, a thin shell of ZnSe was shown to increase the QY of InP significantly, which was then isolated for purification and reconstituted for subsequent thicker shell growth that resulted in near-unity QY InP-based QDs.7 In the case of thin ZnSe-shelled InP QDs with ZnO or GaO_x interlayers, we observed improved linewidths from 230 to 215 meV for the GaO_x interface system, while an increase in PL QY was observed for the ZnO interface QDs (Figure 6a) from 22 to 33% compared to the control InP/ZnSe QD sample. While InP/ZnO/ZnSe QDs showed fixed PL max compared to InP/ZnSe, InP/GaO_x/ZnSe QDs were redshifted by 21 nm.

To further probe these systems, we measured P oxidation by P XES (Figures 7 and S16). ODE-Se was used as the Se precursor in the synthesis to avoid convolution from additional oxidized P components potentially arising from TOP-Se. It is interesting here to note that the increase in PL QY in InP/ZnO/ZnSe QDs is accompanied by a minimal decrease in the P oxidation (8% vs InP/ZnSe) but the reduction in the linewidth of 15 meV shown by InP/GaO_x/ZnSe QD sample is accompanied by a more significant decrease in the P oxidation by 18%. This may suggest that while the oxidative species are having a beneficial role in the electronic confinement of the InP core, resulting in increased PL QY, effective control of P oxidation during shell growth is needed to minimize linewidth broadening. We hypothesize that the observed improvement in P oxidation in the case of the GaO_x interface may be the result

of larger kinetic barriers associated with ion diffusion in this system. The thermodynamic favorability for Ga-P bond over Ga-O bond was previously considered in developing a rationale for the unexpected result where Ga as a dopant was calculated to favor internal bulk sites of the InP magic-sized cluster lattice, unlike heterovalent dopants such as Cd and Zn, which preferred surface sites. Ga may be important in preventing P migration into the ZnSe shell that coincides with the modest narrowing of the linewidth. In a previous study, a subpopulation of In and P atoms incorporated into the ZnSe shell was measured by EDS, implicating such structural defects will have detrimental effects on the optical properties. This highlights the importance of developing a well-controlled interface that connects our understanding of the chemical structure at the atomic level with the resultant PL properties.

Additionally, we grew thicker shells of ZnSe on InP QDs with a ZnO interface. 65 InP QDs were treated with either only ZnEt2 or one full cycle of metal oxide growth (i.e., ZnEt2 and water). Subsequently, ZnSe shells were deposited at 5 equiv relative to total In, resulting in ~2 unit cell monolayers. We observed a more significant increase in the PL after this thick shell growth for QDs with metal oxide at the interface (Figure 6b), from 33% PL QY for InP/ZnSe to 60% with ZnEt₂ treatment and 43% with one full cycle of ZnO growth. Further optimization of this system is necessary to maximize optical properties and fine-tune the interface between the intermediate oxide and the outer insulating shell, but we find these results encouraging. A well-engineered band gap has been shown to suppress Auger processes by delocalizing the wavefunction and softening the confinement potential (quasi-type-II), and a thick inorganic shell can be critical in addressing blinking. 9,36,66 In a type-I system, compositionally gradient shells have been effective in smoothening out the interfacial wavefunction potential.³ Leveraging well-controlled oxidic surface defects and various metal oxides at the interface and at the outermost shell layer could be new avenues to pursue in the fabrication of bright InP-based QDs.

CONCLUSIONS

In this work, we have explored how the identity of the metal oxide interface impacts emissive properties and the oxidative stability of InP QDs using a combination of synthesis, DFT modeling, and physical and electronic structure characterization. Conventional ALD precursors were used in a colloidal system, leading to facile, room-temperature growth of metal oxide shells on InP QDs in a layer-by-layer fashion. This allowed for improved control over the QD surface and core/shell interface with the goal of better controlling the optoelectronic properties of InP-based QDs. Our data support

the formation and growth of ZnO, CdO, and GaO_x shells on InP QDs using this strategy. Interestingly, the first alkyl metal addition step alone forms a thin metal oxide shell, which we hypothesize to be due to the native oxides already present on the InP QD surface. Surface oxide defects in InP QD systems are challenging to control or study, and this work contributes to our understanding of the impact of various metal oxide surfaces on InP QDs and how to leverage this for structural complexity and improved optoelectronic properties. With more optimization, the use of metal oxides as interfaces in core/shell systems and as outer coating layers can be further explored for charge injection, extraction, and transport applications.

METHODS

General Considerations. All glassware was dried in a 160 °C oven overnight prior to use. All reactions, unless otherwise noted, were performed under an inert atmosphere of nitrogen using a glovebox or using standard Schlenk techniques. Indium acetate (99.99%), anhydrous oleic acid (\geq 99%), myristic acid (\geq 99%), anhydrous acetonitrile (99.8%), diethyl zinc (52 wt % based on Zn), and trimethyl aluminum (97%) were purchased from MilliporeSigma and used without further purification. Zinc stearate (tech grade) and selenium powder (99.99%) were purchased from MilliporeSigma and dried before use. Dimethyl cadmium (97%), trimethyl indium (98%), and trimethyl gallium (≥99%) were purchased from Strem and used without further purification. Caution: dimethyl cadmium is extremely toxic and pyrophoric that should be handled with caution and with special care in waste disposal; diethyl zinc, trimethyl aluminum, trimethyl gallium, and trimethyl indium are pyrophoric and should be handled with caution. Toluene was purchased from MilliporeSigma, collected from a solvent still, and stored over activated 3 Å molecular sieves in a glovebox. Acetone (high-performance liquid chromatography (HPLC) grade) was purchased from Fisher and used as purchased. 1-Octadecene (1-ODE, 90%) was purchased from MilliporeSigma, dried over CaH2, distilled, and stored over activated 3 Å molecular sieves in a nitrogen atmosphere glovebox. C₆D₆ was purchased from Cambridge Isotope Laboratories and was similarly dried and stored. Bio-Beads S-X1 for gel permeation chromatography were purchased from Bio-Rad Laboratories and dried under vacuum at elevated temperatures before being stored in a glovebox. Omni Trace nitric acid was purchased from MilliporeSigma and used without further purification. Hydrogen peroxide (30%, ACS grade) was purchased from Fisher and used as purchased. 18 M Ω water was collected from the MilliporeSigma water purification system. P(SiMe₃)₃ was prepared by modifying a literature procedure in which sodium naphthalene was used in place of Na/K alloy. Caution: P(SiMe₃)₃ is a highly pyrophoric liquid that may form toxic phosphine gas upon reaction with air or water and should be handled with caution and care.

Synthesis of InP QDs. Myristate or oleate-capped InP QDs were synthesized from myristate or oleate-capped InP magic-sized clusters (MSC) following a modified preparation. 46,68 While oleate-capped QDs were used for the ¹H NMR studies, both can be used to obtain the same results discussed in the manuscript. Briefly, InP clusters (200 mg myristate MSC or 234 mg oleate MSC, 0.012 mmol) were dissolved in 5 mL of 1-ODE and hot-injected into a flask containing 35 mL of 1-ODE at 300 °C. The growth of the nanocrystals was monitored by UV-vis spectroscopy until the absorbance maximum no longer red-shifted and was halted at 60 min. Once the reaction was complete, the heating mantle was removed to cool down the solution flask. To start purification, 1-ODE was removed by vacuum distillation, and the resulting nanocrystal paste was transferred into a glovebox for precipitation/redissolution cycles using toluene and acetonitrile as solvent and antisolvent, respectively. For further purification, the QD solids were dissolved in toluene and purified twice using gel permeation chromatography in a glovebox following literature procedures. 49,69 Purified InP QDs were dissolved in ~10 mL of toluene and stored as a stock solution in a glovebox. The absorbance value for 100 μ L in 3 mL of toluene was found to be 0.197 for 10 mL of stock solution containing 0.057 mmol of In and used to calculate QD stock concentration.

Colloidal ALD-Inspired Metal Oxide (MOx) Shelling of InP QDs. From a stock solution of InP QDs, a volume containing 0.04 mmol of In was transferred to a vial. More toluene was added to make a total of 2 mL solution. 2 μ L of ZnEt₂ (0.02 mmol) was added. After stirring at room temperature for 1 h, the reaction was evacuated to complete dryness. To continue on the growth cycle with water addition, the QDs were redissolved in toluene and brought outside of the glovebox in a syringe sealed with a septum. The QDs were injected into a 15 mL round-bottom flask on the Schlenk line. Water and acetone were mixed at a 1:7 ratio to facilitate injection of water at sub-microliter volume. This specific ratio additionally allows the injection of the same volume as ZnEt2 for equimolar amounts. After stirring at room temperature for 1 h, the reaction was again evacuated to complete dryness. To continue growth, these steps were repeated for the addition of ZnEt2 and water (refer to Text S1 for the calculation of addition equivalents taking into account the increase in volume). For the growth of cadmium oxide, gallium oxide, aluminum oxide, and indium oxide, 0.02 mmol of CdMe2, GaMe3, AlMe3, and InMe3 were added, respectively. Note that InMe3 is a solid at room temperature and can be added to the reaction accordingly. The reaction can be halted at any point in the growth cycle by evacuating the system and discontinuing further additions.

Synthesis of InP/ZnSe QDs. Thin shelling of ZnSe was adapted from a literature preparation method.⁷ From a stock solution of InP QDs, a volume containing 0.1 mmol of In was transferred to a vial and dried under reduced pressure. The QD solids were redissolved in 3 mL of 1-ODE, injected into an evacuated flask, and brought up to 270 °C while stirring. Zinc stearate (95 mg, 0.15 mmol, suspended in 0.5 mL of 1-ODE) was injected and stirred for 10 min. ODE-Se (400 μ L, 0.08 mmol, from 0.2 $\dot{\text{M}}$ stock solution) was added, and the reaction temperature was maintained at 270 °C. The reaction was monitored by UV-vis and PL spectroscopy and halted after 20 min. For thicker shelling (5 equiv ZnSe to In) adapted from the literature method, 70 a volume of InP QD stock containing 0.04 mmol of In was dried down and redissolved in 2 mL of 1-ODE. Zinc stearate (126 mg, 0.2 mmol, suspended in 1.5 mL of 1-ODE) was injected and stirred for 40 min at 220 °C. TOP-Se (200 μ L, 0.2 mmol, from 1.0 M stock solution) was added, and the reaction temperature was raised to 300 °C. After 60 min, the reaction flask was cooled to room temperature and 1-ODE was removed by vacuum distillation. The reaction flask was transferred into a glovebox for precipitation/redissolution cycles using toluene and acetonitrile as solvent and antisolvent, respectively.

Synthesis of InP/MO_x/ZnSe QDs. InP/ZnSe QDs with metal oxide interfaces were prepared following the same steps for making InP/ZnSe QDs, after the QDs were treated with alkyl metal or one cycle of alkyl metal and water. QD solids were redissolved in 3 mL of 1-ODE and injected into an evacuated flask to start ZnSe shelling as described above.

Synthesis of InP/ZnO/SiO₂. Silica shelling of metal-oxide-shelled InP QDs was necessary to stabilize the QD sample under an electron beam for EDS imaging. Adapting from a literature preparation method, 71 InP/ZnO QDs (0.04 mmol of In) were first suspended in 9 mL of cyclohexane. Then, 1.3 mL of Igepal CO-520 (surfactant) and 150 μ L of ammonia (20%, catalyst) were added to the suspension. The cloudy mixture was sonicated for 10 min. Finally, 200 μ L of tetraethyl orthosilicate (TEOS) was added dropwise over 2 min and stirred for 1 day to complete silica shelling of the QDs. The product was precipitated by centrifugation, washed with water twice, and redispersed in water.

Characterization Techniques. ¹H NMR spectra were collected on a 300 MHz Bruker Avance spectrometer. UV—vis spectra were collected on a Cary 5000 spectrophotometer from Agilent. Fluorescence and absolute quantum yield measurements were taken on a Horiba Jobin Yvon FluoroMax-4 fluorescence spectrophotometer with the QuantaPhi integrating sphere accessory. Powder X-ray diffraction spectra were collected on solid films drop-cast onto a Si

wafer using a Bruker D8 Discover diffractometer. QD solids were digested with $\rm H_2O_2$ and nitric acid overnight and diluted with 18 $\rm M\Omega$ water to prepare ICP samples with which ICP-OES was performed using a PerkinElmer Optima 8300. All samples were purified by size-selective purification prior to the analysis and analyzed once except for as-synthesized InP QDs, for which the In/P ratio has been very consistent across at least 10 samples prepared at varying concentrations. Transmission electron microscopy (TEM) images were collected on an FEI Tecnai G2 F20 microscope at 200 kV. TEM samples were prepared by spotting 3 $\mu \rm L$ of a dilute solution of QDs dispersed in toluene onto an ultrathin carbon on holey carbon support film purchased from Ted Pella. Size distribution analysis was performed on >300 individual NCs per sample.

X-ray Emission Spectroscopy. P K α and K β XES measurements were performed on a laboratory spectrometer described in Abramson with a design similar to that of Holden et al., 73 and where the methodology of Stein et al.¹⁸ was used for estimating the oxidation state. The spectrometer is set up in a N2-filled glovebox and uses a low-power, unfocused X-ray tube (Varex VF-80, 100 W) to illuminate the sample, whose emitted X-rays are analyzed simultaneously by two 10 cm radius of curvature cylindrical crystal analyzer and coupled to homemade complementary metal oxide semiconductor (CMOS) direct-exposure color X-ray cameras. The two multiplexed spectrometers are tuned to the P K α and K β emission energies, respectively. Data collection followed the methodology from Abramson et al. ⁷² InP QD samples were drop-cast onto Si wafer with a spot size of \sim 5 mm diameter. The K α emission spectra were analyzed using linear combination fitting with the nonlinear leastsquares fitting Python package LMFIT.36 (described in more detail in Stein et al. 18). Briefly, two oxidation state components were fit using bulk GaP (2013.57 eV) and Na₂HPO₄ (2014.55 eV) measurements as reference standards.

Extended X-ray Absorption Fine Structure Spectroscopy. X-ray absorption spectroscopy experiments were conducted on Beamline 20-BM of the Advanced Photon Source at Argonne National Laboratory. 20-BM is a spectroscopy beamline equipped with a Bending Magnet source and Si 111 monochromator. Zinc K-edge XAS data were collected in transmission mode over an energy range of 9460–10 515 eV (200 eV below the Zn-K edge of 9660.76 eV to approximately 855 eV above). A total of 430 data points were collected for each scan.

XAS data processing and analysis were executed using XAS Viewer within the LARCH software package. First, the transmission data were plotted as $\mu(E) = -\log(I_{\rm Transmitted}/I_0)$. Next, four scans each for "InP + ZnEt2" and "InP/ZnO (two cycles)" were deglitched (point removal) and averaged together to reduce the noise level. Only a single scan was available for "InP + Zn stearate" due to beam dropout. Raw $\mu(E)$ for each sample was normalized with linear and quadratic functions for pre- and post-edge energy ranges respectively.

Theory: Choice of Basis and Method. A quasi-spherical InP QD, In₇₇P₇₇ (diameter ~2 nm), was constructed using the bulk zinc blende crystal structure. The undoped structure conformed to a $C_{3\nu}$ symmetry before optimization. InP/MO_x core/shell structures were built from the InP core by exchanging surface In with M (where M = Zn, Cd, Ga, Al) and P with O to form In₃₁P₃₁/M₄₆O₄₆. Ground-state geometric optimizations were performed, and the structures were considered optimized when both the forces [maximum and rootmean-square (rms) of the force 0.000450 and 0.000300 hartree/bohr, respectively] and displacement [maximum and rms displacement 0.00018 and 0.0012 bohr, respectively] values were below the threshold criteria. Surface dangling bonds were terminated using a pseudo-hydrogen capping scheme to compensate surface ions: $\pm 1/3$ to passivate the pure, nonshelled InP QD resulting in an In₇₇P₇₇H₁₀₈ structure, and $\pm 1/2$ to passivate the surface O in the InP/MO_x system. These systems are expected to exhibit quantum confinement (Bohr exciton radius is 10 nm for InP).²⁰ Calculations were conducted using the Gaussian software package⁷⁴ using the Perdew, Burke, and Ernzerhof hybrid functional (PBE0)^{75–77} to compute the Kohn-Sham ground-state electronic structure. The Los Alamos National Lab 2-double ζ (LANL2DZ) pseudopotential and associated

basis sets $^{78-81}$ were used. This combination is able to fairly accurately reproduce the experimentally observed 3.7 eV band gap (computational gap is 3.89 eV, +5% in relation to experiment). The electronic structures of excited states were calculated using time-dependent DFT (TD-DFT) within the linear response framework. $^{82-84}$

ASSOCIATED CONTENT

Data Availability Statement

This manuscript has been deposited on ChemRxiv.⁸⁵

Supporting Information

The Supporting Information is available free of charge at https://pubs.acs.org/doi/10.1021/acs.inorgchem.3c00161.

Additional experimental details, DFT models and calculation details, and supporting characterization (PDF)

In77P77H108.xyz (XYZ)
In77P31O46H108.xyz (XYZ)
In31P31Al46O46H108.xyz (XYZ)
In31P31G46O46H108.xyz (XYZ)
In31P31Ga46O46H108.xyz (XYZ)
In31P31Zn46O46H108.xyz (XYZ)
In31P77Al46H108.xyz (XYZ)
In31P77Cd46H108.xyz (XYZ)
In31P77Ga46H108.xyz (XYZ)
In31P77Zn46H108.xyz (XYZ)
In31P77Zn46H108.xyz (XYZ)
In31P77Zn46H108.xyz (XYZ)
In31P31H50.xyz (XYZ)

AUTHOR INFORMATION

Corresponding Author

Brandi M. Cossairt — Department of Chemistry, University of Washington, Seattle, Washington 98195, United States;
orcid.org/0000-0002-9891-3259; Email: cossairt@uw.edu

Authors

Nayon Park — Department of Chemistry, University of Washington, Seattle, Washington 98195, United States Ryan A. Beck — Department of Chemistry, University of Washington, Seattle, Washington 98195, United States; orcid.org/0000-0002-2953-970X

 Kevin K. Hoang – Department of Chemistry, University of Washington, Seattle, Washington 98195, United States
 Dylan M. Ladd – Department of Materials Science and Engineering, University of Colorado, Boulder, Colorado 80309, United States

Jared E. Abramson – Department of Physics, University of Washington, Seattle, Washington 98195, United States

Ricardo A. Rivera-Maldonado – Department of Chemistry, University of Washington, Seattle, Washington 98195, United

Hao A. Nguyen — Department of Chemistry, University of Washington, Seattle, Washington 98195, United States; orcid.org/0000-0001-6742-1748

Madison Monahan – Department of Chemistry, University of Washington, Seattle, Washington 98195, United States

Gerald T. Seidler – Department of Physics, University of Washington, Seattle, Washington 98195, United States; orcid.org/0000-0001-6738-7930

Michael F. Toney — Department of Materials Science and Engineering, Chemical and Biological Engineering, Renewable and Sustainable Energy Institute, University of Colorado, Boulder, Colorado 80309, United States; orcid.org/0000-0002-7513-1166

Xiaosong Li − Department of Chemistry, University of Washington, Seattle, Washington 98195, United States; orcid.org/0000-0001-7341-6240

Complete contact information is available at: https://pubs.acs.org/10.1021/acs.inorgchem.3c00161

Author Contributions

N.P. and B.M.C. designed the project and executed all of the synthesis and baseline characterization. R.A.B., K.K.H., and X.L. carried out the theory and computational investigations. D.M.L. and M.F.T. carried out the EXAFS data collection and analysis. J.E.A., R.A.R., and G.T.S. carried out the XES data collection and analysis. H.A.N. performed the SiO₂ shelling and TEM. M.M. performed additional supporting TEM.

Notes

The authors declare no competing financial interest.

ACKNOWLEDGMENTS

The authors gratefully acknowledge support from the National Science Foundation under grant no. DMR-2019444 as part of the IMOD STC (N.P., D.M.L., H.A.N., M.F.T., B.M.C.). The computational studies build on work supported by DMR-1719797 as part of the UW Molecular Engineering Materials Center (MEM-C), a Materials Research Science and Engineering Center (R.A.B., K.K.H., X.L.). The X-ray emission experiments were supported by CHE-1904437 (J.E.A., R.A.R., G.T.S.). The authors thank Chengjun Sun at Beamline 20-BM of the Advanced Photon Source for his plentiful advice and assistance in the execution of remote X-ray absorption spectroscopy experiments. This research was also supported through student fellowships by the State of Washington through the University of Washington Clean Energy Institute (N.P.). Part of this work was conducted at the Molecular Analysis Facility, a National Nanotechnology Coordinated Infrastructure site at the University of Washington, which is supported, in part, by the National Science Foundation (grant no. NNCI-1542101). The computational work was facilitated by advanced computational, storage, and networking infrastructure provided by the Hyak supercomputer system and funded by the STF at the University of Washington. We also gratefully acknowledge Hao Nguyen for his work on the TOC graphic.

REFERENCES

- (1) Kovalenko, M. V.; Manna, L.; Cabot, A.; Hens, Z.; Talapin, D. V.; Kagan, C. R.; Klimov, V. I.; Rogach, A. L.; Reiss, P.; Milliron, D. J.; Guyot-Sionnnest, P.; Konstantatos, G.; Parak, W. J.; Hyeon, T.; Korgel, B. A.; Murray, C. B.; Heiss, W. Prospects of Nanoscience with Nanocrystals. *ACS Nano* **2015**, *9*, 1012–1057.
- (2) Shu, Y.; Lin, X.; Qin, H.; Hu, Z.; Jin, Y.; Peng, X. Quantum Dots for Display. *Angew. Chem., Int. Ed.* **2020**, *59*, 22312–22323.
- (3) Jang, E.; Kim, Y.; Won, Y.-H.; Jang, H.; Choi, S.-M. Environmentally Friendly InP-Based Quantum Dots for Efficient Wide Color Gamut Displays. *ACS Energy Lett.* **2020**, *5*, 1316–1327.
- (4) Kagan, C. R.; Bassett, L. C.; Murray, C. B.; Thompson, S. M. Colloidal Quantum Dots as Platforms for Quantum Information Science. *Chem. Rev.* **2021**, *121*, 3186–3233.
- (5) Cao, F.; Wang, S.; Wang, F.; Wu, Q.; Zhao, D.; Yang, X. A Layer-by-Layer Growth Strategy for Large-Size InP/ZnSe/ZnS Core—Shell Quantum Dots Enabling High-Efficiency Light-Emitting Diodes. *Chem. Mater.* **2018**, *30*, 8002–8007.
- (6) Won, Y.-H.; Cho, O.; Kim, T.; Chung, D.-Y.; Kim, T.; Chung, H.; Jang, H.; Lee, J.; Kim, D.; Jang, E. Highly Efficient and Stable

- InP/ZnSe/ZnS Quantum Dot Light-Emitting Diodes. *Nature* **2019**, 575, 634–638.
- (7) Li, Y.; Hou, X.; Dai, X.; Yao, Z.; Lv, L.; Jin, Y.; Peng, X. Stoichiometry-Controlled InP-Based Quantum Dots: Synthesis, Photoluminescence, and Electroluminescence. *J. Am. Chem. Soc.* **2019**, *141*, 6448–6452.
- (8) Li, H.; Zhang, W.; Bian, Y.; Ahn, T. K.; Shen, H.; Ji, B. ZnF2-Assisted Synthesis of Highly Luminescent InP/ZnSe/ZnS Quantum Dots for Efficient and Stable Electroluminescence. *Nano Lett.* **2022**, 22, 4067–4073.
- (9) Toufanian, R.; Piryatinski, A.; Mahler, A. H.; Iyer, R.; Hollingsworth, J. A.; Dennis, A. M. Bandgap Engineering of Indium Phosphide-Based Core/Shell Heterostructures Through Shell Composition and Thickness. *Front. Chem.* **2018**, *6*, No. 567.
- (10) Eren, G. O.; Sadeghi, S.; Bahmani Jalali, H.; Ritter, M.; Han, M.; Baylam, I.; Melikov, R.; Onal, A.; Oz, F.; Sahin, M.; Ow-Yang, C. W.; Sennaroglu, A.; Lechner, R. T.; Nizamoglu, S. Cadmium-Free and Efficient Type-II InP/ZnO/ZnS Quantum Dots and Their Application for LEDs. ACS Appl. Mater. Interfaces 2021, 13, 32022–32030.
- (11) Jo, J.-H.; Jo, D.-Y.; Lee, S.-H.; Yoon, S.-Y.; Lim, H.-B.; Lee, B.-J.; Do, Y. R.; Yang, H. InP-Based Quantum Dots Having an InP Core, Composition-Gradient ZnSeS Inner Shell, and ZnS Outer Shell with Sharp, Bright Emissivity, and Blue Absorptivity for Display Devices. *ACS Appl. Nano Mater.* **2020**, *3*, 1972–1980.
- (12) Lee, S. H.; Kim, Y.; Jang, H.; Min, J. H.; Oh, J.; Jang, E.; Kim, D. The Effects of Discrete and Gradient Mid-Shell Structures on the Photoluminescence of Single InP Quantum Dots. *Nanoscale* **2019**, *11*, 23251–23258.
- (13) Zhang, H.; Ma, X.; Lin, Q.; Zeng, Z.; Wang, H.; Li, L. S.; Shen, H.; Jia, Y.; Du, Z. High-Brightness Blue InP Quantum Dot-Based Electroluminescent Devices: The Role of Shell Thickness. *J. Phys. Chem. Lett.* **2020**, *11*, 960–967.
- (14) Ramasamy, P.; Kim, B.; Lee, M.-S.; Lee, J.-S. Beneficial Effects of Water in the Colloidal Synthesis of InP/ZnS Core—Shell Quantum Dots for Optoelectronic Applications. *Nanoscale* **2016**, *8*, 17159—17168.
- (15) Tessier, M. D.; Baquero, E. A.; Dupont, D.; Grigel, V.; Bladt, E.; Bals, S.; Coppel, Y.; Hens, Z.; Nayral, C.; Delpech, F. Interfacial Oxidation and the Photoluminescence of InP-Based Core/Shell Quantum Dots. *Chem. Mater.* **2018**, *30*, 6877–6883.
- (16) Cros-Gagneux, A.; Delpech, F.; Nayral, C.; Cornejo, A.; Coppel, Y.; Chaudret, B. Surface Chemistry of InP Quantum Dots: A Comprehensive Study. *J. Am. Chem. Soc.* **2010**, *132*, 18147–18157.
- (17) Virieux, H.; Le Troedec, M.; Cros-Gagneux, A.; Ojo, W.-S.; Delpech, F.; Nayral, C.; Martinez, H.; Chaudret, B. InP/ZnS Nanocrystals: Coupling NMR and XPS for Fine Surface and Interface Description. *J. Am. Chem. Soc.* **2012**, *134*, 19701–19708.
- (18) Stein, J. L.; Holden, W. M.; Venkatesh, A.; Mundy, M. E.; Rossini, A. J.; Seidler, G. T.; Cossairt, B. M. Probing Surface Defects of InP Quantum Dots Using Phosphorus $K\alpha$ and $K\beta$ X-ray Emission Spectroscopy. *Chem. Mater.* **2018**, *30*, *6377*–*6388*.
- (19) Guzelian, A. A.; Katari, J. E. B.; Kadavanich, A. V.; Banin, U.; Hamad, K.; Juban, E.; Alivisatos, A. P.; Wolters, R. H.; Arnold, C. C.; Heath, J. R. Synthesis of Size-Selected, Surface-Passivated InP Nanocrystals. *J. Phys. Chem. A* **1996**, *100*, 7212–7219.
- (20) Cho, E.; Kim, T.; Choi, S.; Jang, H.; Min, K.; Jang, E. Optical Characteristics of the Surface Defects in InP Colloidal Quantum Dots for Highly Efficient Light-Emitting Applications. ACS Appl. Nano Mater. 2018, 1, 7106–7114.
- (21) Van Avermaet, H.; Schiettecatte, P.; Hinz, S.; Giordano, L.; Ferrari, F.; Nayral, C.; Delpech, F.; Maultzsch, J.; Lange, H.; Hens, Z. Full-Spectrum InP-Based Quantum Dots with Near-Unity Photoluminescence Quantum Efficiency. *ACS Nano* **2022**, *16*, 9701–9712.
- (22) Janke, E. M.; Williams, N. E.; She, C.; Zherebetskyy, D.; Hudson, M. H.; Wang, L.; Gosztola, D. J.; Schaller, R. D.; Lee, B.; Sun, C.; Engel, G. S.; Talapin, D. V. Origin of Broad Emission Spectra in InP Quantum Dots: Contributions from Structural and Electronic Disorder. J. Am. Chem. Soc. 2018, 140, 15791–15803.

- (23) Vikram, A.; Zahid, A.; Bhargava, S. S.; Jang, H.; Sutrisno, A.; Khare, A.; Trefonas, P.; Shim, M.; Kenis, P. J. A. Unraveling the Origin of Interfacial Oxidation of InP-Based Quantum Dots: Implications for Bioimaging and Optoelectronics. *ACS Appl. Nano Mater.* **2020**, *3*, 12325–12333.
- (24) Cui, J.; Beyler, A. P.; Marshall, L. F.; Chen, O.; Harris, D. K.; Wanger, D. D.; Brokmann, X.; Bawendi, M. G. Direct Probe of Spectral Inhomogeneity Reveals Synthetic Tunability of Single-Nanocrystal Spectral Linewidths. *Nat. Chem.* **2013**, *5*, 602–606.
- (25) Yazdani, N.; Volk, S.; Yarema, O.; Yarema, M.; Wood, V. Size, Ligand, and Defect-Dependent Electron—Phonon Coupling in Chalcogenide and Perovskite Nanocrystals and Its Impact on Luminescence Line Widths. ACS Photonics 2020, 7, 1088—1095.
- (26) Hazarika, A.; Fedin, I.; Hong, L.; Guo, J.; Srivastava, V.; Cho, W.; Coropceanu, I.; Portner, J.; Diroll, B. T.; Philbin, J. P.; Rabani, E.; Klie, R.; Talapin, D. V. Colloidal Atomic Layer Deposition with Stationary Reactant Phases Enables Precise Synthesis of "Digital" II—VI Nano-Heterostructures with Exquisite Control of Confinement and Strain. J. Am. Chem. Soc. 2019, 141, 13487–13496.
- (27) Ithurria, S.; Talapin, D. V. Colloidal Atomic Layer Deposition (c-ALD) Using Self-Limiting Reactions at Nanocrystal Surface Coupled to Phase Transfer between Polar and Nonpolar Media. *J. Am. Chem. Soc.* **2012**, *134*, 18585–18590.
- (28) Loiudice, A.; Strach, M.; Saris, S.; Chernyshov, D.; Buonsanti, R. Universal Oxide Shell Growth Enables in Situ Structural Studies of Perovskite Nanocrystals during the Anion Exchange Reaction. *J. Am. Chem. Soc.* **2019**, *141*, 8254–8263.
- (29) Segura Lecina, O.; Hope, M. A.; Venkatesh, A.; Björgvinsdóttir, S.; Rossi, K.; Loiudice, A.; Emsley, L.; Buonsanti, R. Colloidal-ALD-Grown Hybrid Shells Nucleate via a Ligand–Precursor Complex. *J. Am. Chem. Soc.* **2022**, *144*, 3998–4008.
- (30) Sayevich, V.; Robinson, Z. L.; Kim, Y.; Kozlov, O. V.; Jung, H.; Nakotte, T.; Park, Y.-S.; Klimov, V. I. Highly Versatile Near-Infrared Emitters Based on an Atomically Defined HgS Interlayer Embedded into a CdSe/CdS Quantum Dot. *Nat. Nanotechnol.* **2021**, *16*, 673–679.
- (31) Snee, P. T. DFT Calculations of InP Quantum Dots: Model Chemistries, Surface Passivation, and Open-Shell Singlet Ground States. *J. Phys. Chem. C* **2021**, *125*, 11765–11772.
- (32) Rodosthenous, P.; Gómez-Campos, F. M.; Califano, M. Tuning the Radiative Lifetime in InP Colloidal Quantum Dots by Controlling the Surface Stoichiometry. *J. Phys. Chem. Lett.* **2020**, *11*, 10124–10130
- (33) Rusishvili, M.; Wippermann, S.; Talapin, D. V.; Galli, G. Stoichiometry of the Core Determines the Electronic Structure of Core—Shell III—V/II—VI Nanoparticles. *Chem. Mater.* **2020**, 32, 9798—9804.
- (34) Hussein, M. T.; Kasim, T.; Abdulsattar, M. A.; Kaka, A. K. Density Functional Theory Study of InP Quantum Dot and Oxidized Surface. *Int. J. Appl. Innovation Eng. Manage.* **2014**, *3*, 1–8.
- (35) Chandrasekaran, V.; Tessier, M. D.; Dupont, D.; Geiregat, P.; Hens, Z.; Brainis, E. Nearly Blinking-Free, High-Purity Single-Photon Emission by Colloidal InP/ZnSe Quantum Dots. *Nano Lett.* **2017**, *17*, 6104–6109.
- (36) Dennis, A. M.; Buck, M. R.; Wang, F.; Hartmann, N. F.; Majumder, S.; Casson, J. L.; Watt, J. D.; Doorn, S. K.; Htoon, H.; Sykora, M.; Hollingsworth, J. A. Role of Interface Chemistry in Opening New Radiative Pathways in InP/CdSe Giant Quantum Dots with Blinking-Suppressed Two-Color Emission. *Adv. Funct. Mater.* 2019, 29, No. 1809111.
- (37) Efros, A. L.; Nesbitt, D. J. Origin and Control of Blinking in Quantum Dots. *Nat. Nanotechnol.* **2016**, *11*, 661–671.
- (38) Lingerfelt, D. B.; Williams-Young, D. B.; Petrone, A.; Li, X. Direct Ab Initio (Meta-)Surface-Hopping Dynamics. *J. Chem. Theory Comput.* **2016**. *12*. 935–945.
- (39) Avouris, P.; Gelbart, W. M.; El-Sayed, M. A. Nonradiative Electronic Relaxation under Collision-Free Conditions. *Chem. Rev.* 1977, 77, 793–833.

- (40) Send, R.; Furche, F. First-Order Nonadiabatic Couplings from Time-Dependent Hybrid Density Functional Response Theory: Consistent Formalism, Implementation, and Performance. *J. Chem. Phys.* **2010**, 132, No. 044107.
- (41) Kim, K.-H.; Jo, J.-H.; Jo, D.-Y.; Han, C.-Y.; Yoon, S.-Y.; Kim, Y.; Kim, Y.-H.; Ko, Y. H.; Kim, S. W.; Lee, C.; Yang, H. Cation-Exchange-Derived InGaP Alloy Quantum Dots toward Blue Emissivity. *Chem. Mater.* **2020**, *32*, 3537.
- (42) Srivastava, V.; Kamysbayev, V.; Hong, L.; Dunietz, E.; Klie, R. F.; Talapin, D. V. Colloidal Chemistry in Molten Salts: Synthesis of Luminescent In1–XGaxP and In1–XGaxAs Quantum Dots. *J. Am. Chem. Soc.* **2018**, *140*, 12144.
- (43) Schneider, R. P.; Jones, E. D.; Lott, J. A.; Bryan, R. P. Photoluminescence Linewidths in Metalorganic Vapor Phase Epitaxially Grown Ordered and Disordered InAlGaP Alloys. *J. Appl. Phys.* **1992**, *72*, 5397–5400.
- (44) Stein, J. L.; Mader, E. A.; Cossairt, B. M. Luminescent InP Quantum Dots with Tunable Emission by Post-Synthetic Modification with Lewis Acids. *J. Phys. Chem. Lett.* **2016**, *7*, 1315–1320.
- (45) Hanrahan, M. P.; Stein, J. L.; Park, N.; Cossairt, B. M.; Rossini, A. J. Elucidating the Location of Cd2+ in Post-Synthetically Treated InP Quantum Dots Using Dynamic Nuclear Polarization 31P and 113Cd Solid-State NMR Spectroscopy. *J. Phys. Chem. C* **2021**, *125*, 2956.
- (46) Gary, D. C.; Terban, M. W.; Billinge, S. J. L.; Cossairt, B. M. Two-Step Nucleation and Growth of InP Quantum Dots via Magic-Sized Cluster Intermediates. *Chem. Mater.* **2015**, *27*, 1432–1441.
- (47) Park, N.; Eagle, F. W.; DeLarme, A. J.; Monahan, M.; LoCurto, T.; Beck, R.; Li, X.; Cossairt, B. M. Tuning the Interfacial Stoichiometry of InP Core and InP/ZnSe Core/Shell Quantum Dots. *J. Chem. Phys.* **2021**, *155*, No. 084701.
- (48) Shen, Y.; Gee, M. Y.; Tan, R.; Pellechia, P. J.; Greytak, A. B. Purification of Quantum Dots by Gel Permeation Chromatography and the Effect of Excess Ligands on Shell Growth and Ligand Exchange. *Chem. Mater.* **2013**, 25, 2838–2848.
- (49) Roberge, A.; Stein, J. L.; Shen, Y.; Cossairt, B. M.; Greytak, A. B. Purification and In Situ Ligand Exchange of Metal-Carboxylate-Treated Fluorescent InP Quantum Dots via Gel Permeation Chromatography. *J. Phys. Chem. Lett.* **2017**, *8*, 4055–4060.
- (50) Chen, P. E.; Anderson, N. C.; Norman, Z. M.; Owen, J. S. Tight Binding of Carboxylate, Phosphonate, and Carbamate Anions to Stoichiometric CdSe Nanocrystals. *J. Am. Chem. Soc.* **2017**, *139*, 3227–3236.
- (51) Gary, D. C.; Flowers, S. E.; Kaminsky, W.; Petrone, A.; Li, X.; Cossairt, B. M. Single-Crystal and Electronic Structure of a 1.3 Nm Indium Phosphide Nanocluster. *J. Am. Chem. Soc.* **2016**, *138*, 1510–1513.
- (52) Zhao, Q.; Kulik, H. J. Electronic Structure Origins of Surface-Dependent Growth in III–V Quantum Dots. *Chem. Mater.* **2018**, *30*, 7154–7165.
- (53) Pourret, A.; Guyot-Sionnest, P.; Elam, J. W. Atomic Layer Deposition of ZnO in Quantum Dot Thin Films. *Adv. Mater.* **2009**, 21, 232–235.
- (54) Tsui, E. Y.; Hartstein, K. H.; Gamelin, D. R. Selenium Redox Reactivity on Colloidal CdSe Quantum Dot Surfaces. *J. Am. Chem. Soc.* **2016**, *138*, 11105–11108.
- (55) Holder, C. F.; Schaak, R. E. Tutorial on Powder X-Ray Diffraction for Characterizing Nanoscale Materials. *ACS Nano* **2019**, 13, 7359–7365.
- (56) Calvin, J. J.; Kaufman, T. M.; Sedlak, A. B.; Crook, M. F.; Alivisatos, A. P. Observation of Ordered Organic Capping Ligands on Semiconducting Quantum Dots via Powder X-Ray Diffraction. *Nat. Commun.* **2021**, *12*, No. 2663.
- (57) Trigg, E. B. *DebyeByPy*; GitHub, Inc., 2015. http://github.com/etrigg/DebyeByPy.
- (58) Ping, L. K.; Berhanuddin, D. D.; Mondal, A. K.; Menon, P. S.; Mohamed, M. A. Properties and Perspectives of Ultrawide Bandgap Ga2O3 in Optoelectronic Applications. *Chin. J. Phys.* **2021**, 73, 195–212.

- (59) Newville, M. Larch: An Analysis Package for XAFS and Related Spectroscopies. J. Phys.: Conf. Ser. 2013, 430, No. 012007.
- (60) Hughes, K. E.; Stein, J. L.; Friedfeld, M. R.; Cossairt, B. M.; Gamelin, D. R. Effects of Surface Chemistry on the Photophysics of Colloidal InP Nanocrystals. *ACS Nano* **2019**, *13*, 14198–14207.
- (61) Jain, A.; Ong, S. P.; Hautier, G.; Chen, W.; Richards, W. D.; Dacek, S.; Cholia, S.; Gunter, D.; Skinner, D.; Ceder, G.; Persson, K. A. Commentary: The Materials Project: A Materials Genome Approach to Accelerating Materials Innovation. *APL Mater.* **2013**, *1*, No. 011002.
- (62) Kim, S.; Kim, T.; Kang, M.; Kwak, S. K.; Yoo, T. W.; Park, L. S.; Yang, I.; Hwang, S.; Lee, J. E.; Kim, S. K.; Kim, S.-W. Highly Luminescent InP/GaP/ZnS Nanocrystals and Their Application to White Light-Emitting Diodes. *J. Am. Chem. Soc.* **2012**, *134*, 3804–3809.
- (63) Sadeghi, S.; Bahmani Jalali, H.; Melikov, R.; Ganesh Kumar, B.; Mohammadi Aria, M.; Ow-Yang, C. W.; Nizamoglu, S. Stokes-Shift-Engineered Indium Phosphide Quantum Dots for Efficient Luminescent Solar Concentrators. ACS Appl. Mater. Interfaces 2018, 10, 12975–12982.
- (64) Taylor, M. G.; Kulik, H. J. Mapping the Origins of Surface- and Chemistry-Dependent Doping Trends in III–V Quantum Dots with Density Functional Theory. *Chem. Mater.* **2021**, *33*, 7113–7123.
- (65) Reid, K. R.; McBride, J. R.; Freymeyer, N. J.; Thal, L. B.; Rosenthal, S. J. Chemical Structure, Ensemble and Single-Particle Spectroscopy of Thick-Shell InP—ZnSe Quantum Dots. *Nano Lett.* **2018**, *18*, 709—716.
- (66) Hollingsworth, J. A.; Htoon, H.; McBride, J.; Orfield, N. J.; Mishra, N.; Hanson, C. J.; Click, S. M.; Singh, A. Suppressed-Blinking Green (and Infrared)-Emitting "Giant" Quantum Dots (GQDs): From Synthesis to Structure to Function; Los Alamos National Laboratory: Los Alamos, NM, 2017.
- (67) Gary, D. C.; Cossairt, B. M. Role of Acid in Precursor Conversion During InP Quantum Dot Synthesis. *Chem. Mater.* **2013**, 25, 2463–2469.
- (68) Park, N.; Monahan, M.; Ritchhart, A.; Friedfeld, M. R.; Cossairt, B. M. Synthesis of In37P20(O2CR)51 Clusters and Their Conversion to InP Quantum Dots. *J. Visualized Exp.* **2019**, *147*, No. e59425.
- (69) Shen, Y.; Roberge, A.; Tan, R.; Gee, M. Y.; Gary, D. C.; Huang, Y.; Blom, D. A.; Benicewics, B. C.; Cossairt, B. M.; Greytak, A. B. Gel Permeation Chromatography as a Multifunctional Processor for Nanocrystal Purification and On-Column Ligand Exchange Chemistry. *Chem. Sci.* **2016**, *7*, 5671–5679.
- (70) Lim, J.; Bae, W. K.; Lee, D.; Nam, M. K.; Jung, J.; Lee, C.; Char, K.; Lee, S. InP@ZnSeS, Core@Composition Gradient Shell Quantum Dots with Enhanced Stability. *Chem. Mater.* **2011**, 23, 4459–4463.
- (71) Darbandi, M.; Lu, W.; Fang, J.; Nann, T. Silica Encapsulation of Hydrophobically Ligated PbSe Nanocrystals. *Langmuir* **2006**, 22, 4371–4375.
- (72) Abramson, J. E.; Holden, W. M.; Rivera, R. A.; Velian, A.; Cossairt, B. M.; Seidler, G. T. Laboratory X-ray Emission Spectrometer for Phosphorus $K\alpha$ and $K\beta$ of Air-Sensitive Samples. *J. Anal. At. Spectrom.* **2023**, DOI: 10.1039/D3JA00053B.
- (73) Holden, W. M.; Hoidn, O. R.; Ditter, A. S.; Seidler, G. T.; Kas, J.; Stein, J. L.; Cossairt, B. M.; Kozimor, S. A.; Guo, J.; Ye, Y.; Marcus, M. A.; Fakra, S. A Compact Dispersive Refocusing Rowland Circle X-ray Emission Spectrometer for Laboratory, Synchrotron, and XFEL Applications. *Rev. Sci. Instrum.* 2017, 88, No. 073904.
- (74) Frisch, M. J.; Trucks, G. W.; Schlegel, H. B.; Scuseria, G. E.; Robb, M. A.; Cheeseman, J. R.; Scalmani, G.; Barone, V.; Petersson, G. A.; Nakatsuji, H.; Li, X.; Caricato, M.; Marenich, A. V.; Bloino, J.; Janesko, B. G.; Gomperts, R.; Mennucci, B.; Hratchian, H. P.; Ortiz, J. V.; Izmaylov, A. F.; Sonnenberg, J. L.; Williams-Young, D.; Ding, F.; Lipparini, F.; Egidi, F.; Goings, J.; Peng, B.; Petrone, A.; Henderson, T.; Ranasinghe, D.; Zakrzewski, V. G.; Gao, J.; Rega, N.; Zheng, G.; Liang, W.; Hada, M.; Ehara, M.; Toyota, K.; Fukuda, R.; Hasegawa, J.; Ishida, M.; Nakajima, T.; Honda, Y.; Kitao, O.; Nakai, H.; Vreven, T.;

- Throssell, K.; Montgomery, J. A., Jr.; Peralta, J. E.; Ogliaro, F.; Bearpark, M. J.; Heyd, J. J.; Brothers, E. N.; Kudin, K. N.; Staroverov, V. N.; Keith, T. A.; Kobayashi, R.; Normand, J.; Raghavachari, K.; Rendell, A. P.; Burant, J. C.; Iyengar, S. S.; Tomasi, J.; Cossi, M.; Millam, J. M.; Klene, M.; Adamo, C.; Cammi, R.; Ochterski, J. W.; Martin, R. L.; Morokuma, K.; Farkas, O.; Foresman, J. B.; Fox, D. J. *Gaussian 16*, revision B.01; Gaussian, Inc., 2016.
- (75) Ernzerhof, M.; Scuseria, G. E. Assessment of the Perdew–Burke–Ernzerhof Exchange-Correlation Functional. *J. Chem. Phys.* **1999**, *110*, 5029–5036.
- (76) Adamo, C.; Barone, V. Toward Reliable Density Functional Methods without Adjustable Parameters: The PBE0 Model. *J. Chem. Phys.* **1999**, *110*, 6158–6170.
- (77) Perdew, J. P.; Burke, K.; Ernzerhof, M. Errata: Generalized Gradient Approximation Made Simple [Phys. Rev. Lett. 77, 3865 (1996)]. Phys. Rev. Lett. 1997, 78, 1396.
- (78) Dunning, T. H., Jr.; Hay, P. J. In Methods of Electronic Structure Theory; Schaefer, H. F., III, Ed.; Plenum Press: New York, 1977; Vol.
- (79) Wadt, W. R.; Hay, P. J. Ab Initio Effective Core Potentials for Molecular Calculations. Potentials for Main Group Elements Na to Bi. *J. Chem. Phys.* **1985**, *82*, 284–298.
- (80) Hay, P. J.; Wadt, W. R. Ab Initio Effective Core Potentials for Molecular Calculations. Potentials for the Transition Metal Atoms Sc to Hg. *J. Chem. Phys.* **1985**, *82*, 270–283.
- (81) Hay, P. J.; Wadt, W. R. Ab Initio Effective Core Potentials for Molecular Calculations. Potentials for K to Au Including the Outermost Core Orbitals. *J. Chem. Phys.* **1985**, 82, 299–310.
- (82) Casida, M. E. In Recent Advances in Density Functional Methods: Part I; Chong, D. P., Ed.; World Scientific: Singapore, 1995; Vol. 1.
- (83) Dreuw, A.; Head-Gordon, M. Single-Reference Ab Initio Methods for the Calculation of Excited States of Large Molecules. *Chem. Rev.* **2005**, *105*, 4009–4037.
- (84) Stratmann, R. E.; Scuseria, G. E.; Frisch, M. J. An Efficient Implementation of Time-Dependent Density-Functional Theory for the Calculation of Excitation Energies of Large Molecules. *J. Chem. Phys.* 1998, 109, 8218–8224.
- (85) Park, N.; Beck, R.; Hoang, K.; Ladd, D.; Abramson, J.; Rivera, R.; Nguyen, H.; Monahan, M.; Seidler, G.; Toney, M.; Li, X.; Cossairt, B. Colloidal, Room Temperature Growth of Metal Oxide Shells on InP Quantum Dots; ChemRxiv, 2022, DOI: 10.26434/chemrxiv-2022-73k.